51st AIAA Aerospace Sciences Meeting including the New Horizons Forum and Aerospace Exposition
07 - 10 January 2013, Grapevine (Dallas/Ft. Worth Region), Texas

AIAA 2013-0266

Turbulence Structure and Wall Signature in Hypersonic Turbulent Boundary Layer

Yin-Chiu Kan*, Clara Helm†, M. Pino Martín‡

We demonstrate that a similar type of large-scale coherent structures, elongated and low-speed features, that are found in subsonic experiments, are present in our supersonic and hypersonic turbulent boundary layer datasets from direct numerical simulation (DNS). Contour plots of the reconstructed streamwise velocity fluctuation from the most energetic proper orthogonal decomposition (POD) modes show the existence of very long low-momentum regions in the logarithmic layer. Furthermore, the 'superstructure' in the logarithmic layer is found to have a modulating effect on the small-scale motions in the viscous sublayer. Also, we present a physically based automated technique to track and study hairpin packets, as well as their wall signatures and their association with superstructures. Statistical correlations and a geometric algorithm are combined to identify the hairpin packets and their wall signatures. In addition, an activity tracking algorithm that is developed based on feature-Petri net, a mathematical modeling language for the description of distributed systems, is employed to track individual packets and their wall signatures over space and time.

I. Introduction

Previous experimental and numerical studies have provided evidence of large-scale coherent vortical motions, or coherent structures, in turbulent wall-bounded flows. In 1952, Theodorsen[1] postulated the existence of hairpin vortex. He used a simple flow structure (shown in see Figure 1(a)) to explain the formation of low-speed streamwise streaks and the ejection of near-wall low-momentum fluid into higher-momentum regions farther from the wall. In 1981, Head and Bandyopadhyay[2] found experimental evidence of individual hairpin vortices stacking and organizing into packets in the streamwise direction in turbulent boundary layers over a large range of Reynolds numbers ($500 < \mathrm{Re}_\theta < 17500$), and they observed that the hairpin vortex heads forms an envelope of a 15° to 20° downstream leaning angle with respect to the wall. In 2000, Adrian, Meinhart, and Tomkins[3] proposed a hairpin packet model, where the hairpins align in the streamwise direction and organize into packets, as observed by Head and Bandyopadhya. In this model, the low momentum regions are enclosed by hairpin packets. Therefore, hairpin heads and counter-rotating legs within the packets align in the streamwise direction and induce the low-momentum, very large-scale motions (VLSM) observed by Jiménez,[4] Hutchins and Marusic[5] and Kim and Adrian,[6] see Figure 1(b). Moreover, Adrian *et al.*[3] proposed that hairpin packets grow in size as they evolve and result in a nested packets that consisting of hairpins or cane-type vortices growing up from the wall due to the older packets giving rise to younger and slower packets. Adrian *et al.*[3] also found that hairpins vortices are mostly appear as asymmetric cane-like vortices. Following this work, the term "hairpin" is used throughout to refer both to symmetric horseshoe-like vortices and asymmetric cane-like vortices.

Turbulence structures in boundary layers have been mostly studied in the subsonic flow regime (for example, Tomkins and Adrian;[7] del Álamo and Jiménez;[8] Ganapathisubramani, Longmire and Marusic;[9] del Álamo *et al.*;[10] del Álamo *et al.*;[11] Guala, Hommena and Adrian;[12] Hambleton, Hutchins and Marusic;[13] Flores *et al.*;[14] Balakumar and Adrian;[15] Hutchins and Marusic[5] and Mathis, Hutchins and Marusic[16]). In contrast to supersonic and hypersonic flow regimes, limited studies could be found due to the lack of detailed flow field data, and the studies have been mostly restricted to statistical analysis. For example, Smits *et*

*Graduate Student, Department of Aerospace Engineering, University of Maryland, College Park.
†Graduate Student, Department of Aerospace Engineering, University of Maryland, College Park.
‡AIAA Associate Fellow. Associate Professor, Department of Aerospace Engineering, University of Maryland, College Park.

al.,[17] Spina, Donovan and Smits,[18] and Smits and Dussauge[19] were able to obtain the convection velocity, inclination angle, and length scale of the turbulent structure via space-time correlations. They found that structure properties change with both Mach and Reynolds number. More recently, advances in numerical techniques (Guarini *et al.*;[20] Martin;[21,22] Pirozzoli, Grasso and Gatski;[23] Xu and Martin;[24] Ringuette, Wu and Martin[25] and experimental techniques (Elsinga *et al.*;[26]Schrijer, Scarano and van Oudheusden;[27] van Oudheusden;[28] Humble, Scarano and van Oudheusden[29]) make possible for the acquisition of detailed four dimensional, in time and space, flow field data of supersonic/hypersonic turbulent boundary layers. In particular, both numerical[25,30] and experimental[26,31,32] data at supersonic Mach numbers have shown evidence of VLSM. For instance, Ganapathisubramani, Clemens and Dollings[31] performed wide-field DPIV in a Mach 2 turbulent boundary layer and observed alternating streamwise structures of uniform low- and high-speed fluid in the logarithmic region with lengths exceeding their 8δ field of view. O'Farrell and Martin[33] were able to track the temporal evolution of hairpin packets and their wall signatures over a three-dimensional space and time Mach 3 DNS turbulent boundary layer data.

In this paper, we present a set of analytical tools to study large-scale structures, in particular hairpin packets and their wall signatures, in a Mach 2.9 and a Mach 7.2 spatially developing DNS turbulent boundary layer data. In Section II, we present the direct numerical simulation of Mach 2.9 ($\mathrm{Re}_\tau \approx 650$) and Mach 7.2 ($\mathrm{Re}_\tau \approx 650$) turbulent boundary layers over an adiabatic wall. In Section III, we present methods that are used to examine the existence of "superstructure" at the logarithmic layer. In addition, we summarize the analytical tools and techniques that are used to identify hairpin packets, demonstrate how we distinguish weak, average and strong packets using the combinations of geometric algorithm and statistical methods, and describe the activity tracking algorithm that is used to track evolution hairpin packets and their wall signatures. In Section IV and V, we present the preliminary results and conclusions, respectively.

II. DNS parameters and accuracy

To study the turbulent structures over boundary-layers, we use the spatially developing DNS dataset of a Mach 2.9 and a Mach 7.2 turbulent boundary layers over an adiabatic wall. The inflow boundary condition is provided by the rescaling technique outlined by Xu and Martin.[24] The boundary-layer edge conditions and wall parameters for both cases are given in Table 1, which provide boundary-layer edge Mach number, density and temperature, M_δ, ρ_δ and T_δ, respectively, and boundary-layer properties: momentum thickness (θ), shape factor $\mathrm{H} = \delta^*/\theta$, where δ^* being the displacement thickness, Reynolds number based on momentum thickness, $\mathrm{Re}_\tau = \rho_w u_\tau \delta/\mu_w$, and boundary-layer thickness δ. For both cases, the wall condition is adiabatic.

For the computational domain and grid resolution, the domain size, L/δ_0 where the value δ_0 is shown in table 2, and the number of grid points, N, for both cases are given in table 2, where the superscript $(^+)$ indicates scaling with inner or wall values. We take the streamwise, spanwise, and wall-normal directions to be x, y, and z, respectively. Grid resolutions in the streamwise, spanwise, and wall-normal direction are denoted in table 2 as $\Delta\mathrm{x}^+$, $\Delta\mathrm{y}^+$, and $\Delta\mathrm{z}^+$, respectively. The details of the numerical method are given by Xu and Martin.,[24] and the accuracy of the simulations is validated in Beekman, Priebe, Kan, Martin,[34] and Priebe and Martin.[35] For the temporal tracking, the sampling rate is $1.20{*}10^{-6}$ sec and $1.02{*}10^{-6}$ sec for the Mach 2.9 case and the Mach 7.2 case,respectively, where structures travels approximately 0.1 δ_0 between each sample for both cases

Case	M_δ	ρ_δ(kg/m^3)	T_δ (K)	$\mathrm{T}_w/\mathrm{T}_\delta$	Re_τ	Re_θ	θ(mm)	H	δ(mm)
Mach 2.9	2.91	0.0754	109.06	2.81	390–710	2620–4906	0.45–0.84	5.13	7.03–13.24
Mach 7.2	7.13	0.0765	64.31	10.10	373–575	11441–17682	0.60–0.92	24.23	24.21–37.48

Table 1. Freestream, boundary-layer, and wall parameters for the DNS.

Case	L_x/δ_0	L_y/δ_0	L_z/δ_0	δ_0(mm)	N_x	N_y	N_z	Δ_x^+	Δ_y^+	Δ_z^+	Size
Mach 2.9	59.5	9.91	9.09	6.41	2520	1120	110	8.49	3.18	0.311	$\approx$ 310 Million
Mach 7.2	54.0	9.00	19.7	20.4	2200	924	130	7.91	3.24	0.237	$\approx$ 260 Million

Table 2. Grid resolution and domain size for the DNS. The grid is equispaced in the streamwise and spanwise directions and uses a geometric stretching in the wall normal direction. Here, $\Delta_z^+ = z_2 - z_1$

III. Analytical Tool

A. POD and Modulating Effect of Superstructure

In this section, we examine the existence of 'superstructure' in the logarithmic layer for our datasets via a decomposition method and a statistical method. Baltzer, Adrian, and Wu[36] were able to observe 'superstructure' in the logarithmic layer in an spatially developing DNS data of an incompressible turbulent boundary-layer by performing a three-dimensional proper orthogonal decomposition (POD) analysis. Details of the method can be found in Baltzer, Adrian, and Wu;[36] here, we summarize it. Since boundary-layers are statistically homogeneous and periodic in spanwise direction, POD modes converge to trigonometric functions; thus, fluctuating velocity can be decomposed into Fourier modes (k_y) in the spanwise direction. In terms of the fluctuating velocity in the streamwise and wall-normal direction, they could be decomposed into POD mode (n) that were calculated from a collection of 51 fluctuating velocity flow field snapshots. To retain the large-scale coherent structures, an instantaneous reconstruction streamwise fluctuating velocity flow field could be reconstructed using a set of the most energetic modes (k_y and n). Here, we apply the similar analysis on both the Mach 2.9 and the Mach 7.2 datasets. In Section IVA, we show the results of the reconstructed streamwise velocity fluctuation in the logarithmic layer ($z/\delta_0 = 0.2$) and provide evidence of very-large-scale-motion (VLSM) or 'superstructure' in our datasets.

Mathis, Hutchins and Marusic[37] computed the modulation correlation between the large-scale signals and the small-scale envelope (by Hibert transform) of streamwise velocity at different wall-normal locations, and observed correlation peak occurred at $z^+ = 15$, which indicated that large-scale motions in the logarithmic layer have a modulating effect on the small-scale motions in viscous sublayer. Again, we perform similar analysis to provide evidence of "superstructure" in the Mach 2.9 and Mach 7.2 datasets.

After examining the existence of 'superstructures' in our datasets, we use different analytical tools to identify and track hairpin packets, as previous studies found that 'superstructures' are induced by the hairpin packets. In our analysis, geometric algorithm[25] (discuss in Section III B) and statistical correlations[38] (discuss in Section III C) are used to identify hairpin packets, and activity tracking algorithm by Wang and Silver[39] and Sedat, Silver, Bemis, Martin, and Takle[40] (discuss in Section III E) is employed to track the identified packets as well as their wall signatures temporally and spatially in the DNS data.

B. Geometric Algorithm

The details of geometric algorithm described in Ringuette, Wu and Martin.[25] Here, we summarize it. The algorithm first sweeps each (x, z) plane and searches for head vortices based on two thresholds: (1) the spanwise vorticity is greater than or equal to two standard deviations from the mean ($\omega_y \geq \overline{\omega_y} + 2\sigma(\omega_y)$). (2) the swirling strength is greater than or equal to 4.5 times the mean swirling strength ($\lambda_{ci}^2 \geq 4.5\overline{\lambda_{ci}^2}$). Note that only the region between the buffer layer ($z^+ = 30$) and the boundary layer edge is considered for computing the threshold quantities and finding hairpin packets. In Ringuette, Wu and Martin,[25] average quantities and Reynolds number is nearly constant over the entire DNS datasets. When compared to our cases, our streamwise domain in both cases are at least 5 times larger; thus, average quantities and Reynolds number variation would be significant over the streamwise direction. As a result, we define the mean (over-bar) quantities as Gaussian moving averaging quantities following Equation 1 with streamwise half-width (hw) of $4\delta_0$, which allows mean (over-bar) quantities varies at each streamwise location. After identifying the hairpin heads on each (x, z) plane, two extra geometric criteria based on the proposed model by Adrian, Meinhart, and Tomkins[3] are used to group hairpin heads into ideal packets: (1) hairpin head, or transverse, vortices that are closely spaced ($\leq 0.5\delta$) in the streamwise direction. (2) hairpin head, or transverse, vortices that are arranged in a ramp-like formation with $\leq 45°$ downstream leaning angle relative

to the wall. After conforming hairpin heads into ideal packets, extra criteria is applied on the large structures (wall-normal height $> 0.1\delta$, streamwise distance $> 0.1\delta$) that are identified to assure that hairpin legs do not captured in the hairpin heads searching process. Essentially, the scheme performs a least-squares-fit through the identified points of the large structures, and omits the structure if the angle of the line is less than 25°. This improves the accuracy of the algorithm for picking out hairpin packets, and prevents to accept large, relatively horizontal shear layers with high ω_y or λ_{ci}^2. Figure 2, from Ringuette, Wu and Martin.[25] shows the results of the algorithm. Figure 2(a) plots the iso-surfaces of swirling strength for a packet identified by the algorithm. Figure 2(b) plots a slice from the translucent plane highlighted in Figure 2(a) with contours of spanwise vorticity, where the hairpin vortex heads identified by the algorithm are enclosed by the boxes. In addition, Figure 2(c) shows a contour with streamwise velocity on a streamwise-spanwise plane, where tick marks, at two spanwise locations, are indicating the hairpin heads that are identified by the algorithm. From this plot, it provides evidence that hairpin packets do indeed align in the streamwise direction and giving rise to the 'superstructure.' By applying the algorithm to our cases, similar results are observed.

$$\overline{x(i)} = \sum_{k=i-hw}^{i+hw} \omega(k)x(k),\ where\ \omega(k)\ is\ the\ weight\ of\ the\ Gaussian\ window \tag{1}$$

C. Correlation Method

Brown and Thomas[38] were able to use the correlation between the the wall shear stress and streamwise velocity at a single reference location over different wall-normal distances to detect large-scale structures in the boundary layer. From the correlation profile, the correlation peak were found to be at an increasing downstream distance with increasing wall-normal location, which indicated the presence of downstream-leaning coherent structure. In addition, Brown and Thomas[38] used conditional averages to better understand the structures that were found. Essentially, when the correlation at $z/\delta = 0.25$ is greater than twice of the peak average value at the Δx location of the peak, they categorized these data traces as 'strong' events. By averaging on these strong events, they provided evidence of the existence of ramp-like coherent structures in the boundary layer.

In Ringuette, Wu and Martin.,[25] they applied the same method on the DNS data of Mach 3 turbulent boundary layer. They were able to construct the correlation profile over different wall-normal distance using

$$R_{\tau_w(\rho u)}(\Delta x) = 1/(x_2 - x_1) \left\langle \overline{\int_{x_1}^{x_2} \tau_w'(x)(\rho u)'(x+\Delta x)dx} \right\rangle / \tau_{w,RMS}'(\rho u)_{RMS}'. \tag{2}$$

where the over-bar and angle brackets denote spatial (streamwise and spanwise) and temporal averaging, respectively. For the supersonic flow, they performed the correlation between the wall shear stress and streamwise mass flux. Here, we perform the same analysis on both of the Mach 2.9 and Mach 7.2 cases. Figure 3(a), 3(b), 3(c) and 3(d) show the average and enhanced correlations for the Mach 2.9 and Mach 7.2 data, respectively. Using this technique, we are able to conditionally sample the data and categorize the data into weak, average and strong packets.

D. Relationship between the Geometric Algorithm and the Correlation Method

In O'Farrell and Martin,[33] they performed a turbulent structure on a Mach 3 DNS boundary layer data by combining the results of geometric algorithm and Brown and Thomas[38] correlation on a Mach 3 DNS boundary layer data. Essentially, they categorized the average packet structure statistics determined from Brown and Thomas[38] correlation into average-strong, average-average, and average-weak packets as mentioned in Section III C. By applying the Brown and Thomas[38] correlation on the packets that were identified by geometric algorithm, they were able to distinguish the geometric events into average strong-geometric, average-geometric, and weak-geometric packets. Furthermore, they were able to determine the average convection velocity profile of the vortices that belong to identified packets for both geometric algorithm and Brown and Thomas[38] correlation. Details of finding the average convection velocity profile could be found in O'Farrell and Martin[33] and Beekman, Priebe, Ringuette, and Martin.[41] By comparing the average convection velocity profiles determined by geometric algorithm from the velocity profiles determined by the 'enhanced' Brown and Thomas[38] correlation data, they found the relationship between the Geometric Algorithm and the Brown and Thomas[38] correlation. Figure 4 plots the average vortex convection velocity and

the mean flow velocity profiles for the Mach 3 data from O'Farrell and Martin,[33] where the data suggests that the average geometric packets are representative of the strong statistical packets.

E. Activity Tracking Algorithm

O'Farrell and Martin[33] used the Object Segmentation and Feature Tracking (Ostrk2.0) software package[39,42] to identify individual hairpin packets and track their evolution through consecutive flow realizations on DNS data of a Mach 3 turbulent boundary layer. The tracking software performs tasks in three levels, which are Feature Tracking, Grouping, and Group Tracking, on the instantaneous swirling strength fields. To summarize, the tracking software extracts and tracks hairpin or cane-like vortices, based on the user-specified threshold ($4.5\overline{\lambda_{ci}^2}$) at Feature Tracking level and groups hairpin vortices into ideal packets that conform with the criteria of Ringuette, Wu and Martin,[25]at the Grouping level. Finally, the group tracking level is used to temporally track the evolution of packets. Further details on Ostrk2.0 could be found in the User Manual by Liang,[42] and the paper by Wang and Silver.[39] O'Farrell and Martin[33] find that the software mistakenly merge the neighboring vortices into a packets showing unphysical proliferation of packets. Thus, they were not able to obtain satisfactory results from Ostrk2.0.

Recently, Sedat, Silver, Bemis, Martin, and Takle[40] implement one more level, called higher level grouping (see Figure 5(a), onto Ostrk2.0 which performs cross-level interactions of the group tracking level to improve the accuracy of the temporal tracking evolution of packets without unphysical growth. By applying the improved activity tracking algorithm to our Mach 2.9 data, Figure 6 shows an iso-surface of the swirling strength equal to $4.5\overline{\lambda_{ci}^2}$ of a geometrically strong packet in four time realizations.

F. Wall Signatures

Brown and Thomas,[38] and Thomas and Bull[43] performed experiments with incompressible turbulent boundary layers and shown characteristic patterns in the wall-shear stress and wall-pressure, which are hypothesized to be associated with large-scale coherent motions. Figure 7 is a reproduction of a schematic from the paper by Thomas and Bull,[43] which shows a large-scale, coherent motion together with the associated wall shear stress and pressure signatures. In Section IV C, we combine the geometric algorithm, Brown and Thomas correlation, and activity tracking algorithm to temporally track two identified geometrically strong packets, as well as their wall signatures to examine the characteristic patterns of the wall-shear stress and wall-pressure on our datasets.

IV. Preliminary Results

A. Existence of Superstructure

We perform the same three dimensional POD, by Baltzer, Adrian and Wu,[36] that discussed in Section III A on the Mach 2.9 and Mach 7.2 datasets. We decompose 924 spanwise modes (k_y) and 51 POD modes (n) and 1024 spanwise modes (k_y) and 51 POD modes (n) for the Mach 2.9 and the Mach 7.2 datasets, respectively. To filter out the small-scale motions and retain the large-scale motions, energetic modes are kept to reconstruct the velocity fields. k_{th} = 0–200 and n=1–10 are kept in both cases. In terms of the mean turbulent kinetic energy, 42.3% and 44.5% of the mean turbulent kinetic energy are retained for the Mach 2.9 and Mach 7.2 case, respectively. Figure 8(b) and Figure 9(b) show the reconstructed streamwise velocity fluctuation at $z/\delta_0 = 0.2$ for both cases. Very long ;ow-momentum are observed in both cases, which indicates the existence of 'superstructure' in the datasets.

To examine the modulating effect of superstructure, we perform a similar analysis, by Mathis, Hutchins and Marusic,[37] that is discussed in Section III A on both datasets. Further details are given in Helm and Martin.[44] As an example, Figure 10 show the original and filtered temporal signals of streamwise velocity and their envelope (by Hibert transform) in the logarithmic layer ($z^+ = 100$) and in the viscous sublayer ($z^+ = 10$) for the Mach 2.9 case. In Figure 10(c), we could observe the modulating effect between the large-scale in logarithmic layer and the small-scale in viscous sublayer. To further examine the modulating effect, we compute the modulation correlation between large-scale signal (fixed at $z^+ = 100$) and the small-scale envelope at different wall-normal locations. Figure 11 shows small-scale modulation in the viscous sublayer and in the logarithmic layer for both cases. As shown in Figure 11, the highest correlation occurs in the logarithmic region ($z^+ \approx 10$) for both datasets, which implies the existence of the modulating effect and the

presence of the large-scale coherent structures in the logarithmic region.

B. Packet Convection Velocities

By applying the Brown and Thomas[38] correlation analysis on the Mach 2.9 and Mach 7.2 datasets, the correlation profiles show that structures with downstream leaning angle exist in both datasets (shown in Figure 3(a) and 3(c). Furthermore, we are able to obtain the packet convection velocities by averaging the instantaneous identified vortices at each wall-normal location. As discussed in Section III B, the Reynolds number variation is significant over streamwise direction; therefore, we sample the velocity profiles with a subset of data. Here, we choose the sub-volume where $\mathrm{Re}_\tau \approx 560$ for both bases, where the stations correspond to $24 \leq x/\delta_0 \leq 28$ and $46 \leq x/\delta_0 \leq 54$ for the Mach 2.9 case and the Mach 7.2 case, respectively. Figure 12 shows the statistically 'strong' and geometrically 'average' vortex convection velocity profiles by the conditional averaging from statistical correlation method. The mean velocity profiles are included for reference. Consistent with the result found in O'Farrell and Martin,[33] all statistical and geometrical 'strong' packets induced greater drag. Weak events are considered unimportant and are found to be convect approximately with the mean flow in both cases. Consistently with our previous work, the 'strong' packets in the Mach 7.2 case convect slower than the mean velocity. Furthermore, it could be seen that the convection velocity profiles of the geometrically 'average' packets are nearly identical to convection velocity profiles of the statistically 'strong' packets. This further supports that ideal geometric packets are representative of strong events across the Mach number varying data.

C. Packet Tracking and Wall Signatures

We have tracked two geometrically 'strong' hairpin packets using the activity tracking algorithm discussed in section III E. We use this software to followe two geometrically 'strong' hairpin packets, highlighted in solid colors in Figure 13 and Figure 16, in both Mach 2.9 and Mach 7.2 cases. After tracking this packet and watching its evolution, we monitored their wall signatures at two time instances. Figure 14((c),(d)) and Figure 15((c),(d)) show the wall-pressure and the wall-shear stress of the associated packets at a selected time instance and at a time instance where the packets traveled a distance of approximately δ_0. In both figures, visualizations of the identified packets in streamwise-wall normal plane and streamwise-spanwise plane are plotted with iso-surfaces of the swirling strength at $4.5\overline{\lambda_{ci}^2}$. In addition, Figure 17 and Figure 18 plot the same content for the Mach 7.2 case. For all cases shown in Figure 14, 15, 17, and 18, hairpin vortices within the identified packets are cane-like with sets of asymmetric counter rotating legs. Consistent with the hypothesis by Brown and Thomas[38] and Thomas and Bull,[43] a significant peak could be observed in both the wall-shear stress and wall-pressure signals associated with the hairpin legs.

V. Conclusions

Through POD analysis and modulation correlation between the large-scale motions in the logarithmic layer and the small-scale motions in the viscous sublayer, we present 'superstructure' type of motions present from supersonic and hypersonic turbulent boundary layer datasets in direct numerical simulation (DNS). As 'superstructures' are found to be induced by hairpin packets, we demonstrate a number of analytical tools and techniques, such as the Geometric algorithm[25] (discuss in Section III B) and the statistical correlations[38] (discuss in Section III C) to identify hairpin packets. By performing the Brown and Thomas correlations on the 'geometric events' identified by the geometric algorithm, we are able to further categorize the packets identified by the geometric algorithm into 'strong,' 'average,' and 'weak' events.

To further investigate the wall signatures of hairpin packets, we use the activity tracking algorithm by Sedat, Silveris, Bemis, Martin, and Takle39[40] (discuss in Section III E) to track the temporal evolutions of identified geometrically 'strong' packets and their wall signatures. By observing the evolutions, characteristic patterns of wall signatures associated with the hairpin legs, hypothesized by Brown and Thomas[38] and Thomas and Bull,[43] are observed in the supersonic and hypersonic turbulent boundary layer DNS datasets. This further corroborates the modulation of the near wall cycle by the packets populating the superstructures in the logarithmic layers as proposed and observed by Mathis, Hutchins and Marusic[16] and Helm and Martin.[44]

Acknowledgments

This work is supported by the Air Force Office of Scientific Research under grant AF/9550-10-1-0535 "STW 21 - Revitalization of the Hypersonics Testing and Evaluation Workforce."

References

[1]Theodorsen, T., "Mechanism of Turbulence," *Proc. 2nd. Midwestern Conf. on Fluid Mech.*, Ohio State University, Columbus, Ohio, USA, 1952, pp. 1–19.

[2]Head, M. and Bandyopadhyay, P., "New aspects of turbulent boundary-layer structure," *J. Fluid Mech.*, Vol. 107, 1981, pp. 297–338.

[3]Adrian, R., Meinhart, C., and Tomkins, C., "Vortex organization in the outer region of the turbulent boundary layer," *J. Fluid Mech.*, Vol. 422, 2000, pp. 1–54.

[4]Jiménez, J., "The largest scales of turbulent wall flows," *Center for Turbulence Research, Annual Research Briefs*, Stanford University, 1998, pp. 137–154.

[5]Hutchins, N. and Marusic, I., "Evidence of very long meandering features in the logarithmic region of turbulent boundary layers," *J. of Fluid Mechanics*, Vol. 579, 2007, pp. 1–28.

[6]Kim, K. C. and Adrian, R. J., "Very large-scale motion in the outer layer," *Phys. Fluids*, Vol. 11, No. 2, 1999, pp. 417–422.

[7]Tomkins, C. and Adrian, R., "Spanwise structure and scale growth in turbulent boundary layers," *J. Fluid Mech.*, Vol. 490, 2003, pp. 37–74.

[8]del Álamo, J. C. and Jiménez, J., "Spectra of the very large anisotropic scales in turbulent channels," *Phys. Fluids*, Vol. 15, No. 6, 2003, pp. L41–L44.

[9]Ganapathisubramani, B., Longmire, E. K., and Marusic, I., "Characteristics of vortex packets in turbulent boundary layers," *J. Fluid Mech.*, Vol. 478, 2003, pp. 35–46.

[10]del Álamo, J. C., Jiménez, J., Zandonade, P., and Moser, R. D., "Scaling of the energy spectra of turbulent channels," *J. Fluid Mech.*, Vol. 500, 2004, pp. 135–144.

[11]del Álamo, J. C., Jiménez, J., Zandonade, P., and Moser, R. D., "Self-similar vortex clusters in the turbulent logarithmic region," *J. Fluid Mech.*, Vol. 561, 2006, pp. 329–358.

[12]Guala, M., Hommema, S. E., and Adrian, R. J., "Large-scale and very-large-scale motions in turbulent pipe flow," *J. Fluid Mech.*, Vol. 554, 2006, pp. 521–542.

[13]Hambleton, W. T., Hutchins, N., and Marusic, I., "Simultaneous orthogonal-plane particle image velocimetry measurements in a turbulent boundary layer," *J. Fluid Mech.*, Vol. 560, 2006, pp. 53–64.

[14]Flores, O., Jiménez, J., and del Álamo, J. C., "Vorticity organization in the outer layer of turbulent channels with disturbed walls," *J. Fluid Mech.*, Vol. 591, 2007, pp. 145–154.

[15]Balakumar, B. J. and Adrian, R. J., "Large- and very-large-scale motions in channel and boundary-layer flows," *Phil. Trans. R. Soc. A*, Vol. 365, 2007, pp. 665–681.

[16]Mathis, R., Hutchins, N., and Marusic, I., "Large-scale amplitude modulation of the small-scale structures in turbulent boundary layers," *J. Fluid Mech.*, Vol. 628, 2009, pp. 311–337.

[17]Smits, A., Spina, E., Alving, A., Smith, R., Fernando, E., and Donovan, J., "A comparison of the turbulence structure of subsonic and supersonic boundary layers," *Phys. Fluids A*, Vol. 1, 1989, pp. 1865–1875.

[18]Spina, E., Donovan, J., and Smits, A., "On the structure of high-Reynolds number supersonic turbulent boundary layers," *J. Fluid Mech.*, Vol. 222, 1991, pp. 293–327.

[19]Smits, A. J. and Dussauge, J.-P., *Turbulent shear layers in supersonic flow*, Springer, 2nd ed., 2006.

[20]Guarini, S., Moser, R., Shariff, K., and Wray, A., "Direct numerical simulation of supersonic turbulent boundary layer at Mach 2.5," *J. of Fluid Mech.*, Vol. 414, 2000, pp. 1–33.

[21]Martín, M. P., "DNS of hypersonic turbulent boundary layers," *AIAA Paper 2004-2337*, 2004.

[22]Martín, M. P., "Direct numerical simulation of hypersonic turbulent boundary layers. Part 1: Initialization and comparison with experiments," *J. Fluid Mech.*, Vol. 570, 2007, pp. 347–364.

[23]Pirozzoli, S., Grasso, F., and Gatski, T., "Direct numerical simulation and analysis of a spatially evolving supersonic turbulent boundary layer at M=2.25," *Phys. Fluids*, Vol. 16, No. 3, 2004, pp. 530 – 545.

[24]Xu, S. and Martín, M., "Assessment of Inflow Boundary Conditions for Compressible Turbulent Boundary Layers," *Physics of Fluids*, Vol. 16, No. 7, 2004, pp. 2623–2639.

[25]Ringuette, M. J., Wu, M., and Martín, M. P., "Coherent structures in direct numerical simulation of turbulent boundary layers at Mach 3," *J. Fluid Mech.*, Vol. 594, 2008, pp. 59–69.

[26]Elsinga, G., Adrian, R., Van Oudheusden, B., and Scarano, F., "Three-dimensional vortex organization in a high-Reynolds-number supersonic turbulent boundary layer," *J. of Fluid Mech.*, Vol. 644, 2010, pp. 35–60.

[27]Schrijer, F., Scarano, F., and van Oudheusden, B., "Application of PIV in a Mach 7 double-ramp flow," *Experiments in Fluids*, Vol. 41, 2006, pp. 353–363.

[28]van Oudheusden, B., "Principles and application of velocimetry-based planar pressure imaging in compressible flows with shocks," *Experiments in Fluids (electronic Open Access)*, 2008.

[29]Humble, R., Scarano, F., and van Oudheusden, B., "Experimental study of an incident shock wave/turbulent boundary layer interaction using PIV," *AIAA Paper Number*, Vol. number 2006-3361, 2006.

[30]Wu, M. and Martín, M., "Direct numerical simulation of shockwave and turbulent boundary layer interactions over a compression ramp," *AIAA J.*, Vol. 45, 2007, pp. 879–889.

[31]Ganapathisubramani, B., Clemens, N., and Dolling, D., "Large-scale motions in a supersonic turbulent boundary layer," *J. Fluid Mech.*, Vol. 556, 2006, pp. 1–11.

[32]Ganapathisubramani, B., Clemens, N., and Dolling, D., "Effects of upstream boundary layer on the unsteadiness of shock-induced separation," *J. Fluid Mech.*, Vol. 585, 2007, pp. 369–394.

[33]O'Farrel, C. and Martin, M. P., "Chasing Eddies and Their Wall Signature in DNS Data of Turbulent Boundary Layers," *J. Turbuence*, N15, 2010.

[34]Beekman, I., Priebe, S., Kan, Y., and Martin, M. P., "DNS of a Large-Domain, Mach 3 Turbulent Boundary Layer: Turbulence Structure," *AIAA Paper No. 2011-753*, Jan 2011.

[35]Priebe, S. and Martin, M. P., "Low-frequency Unsteadiness in Shock Wave-turbulent Boundary Layer Interaction," 2012, pp. 1–49.

[36]Baltzer, J. R., Adrian, R. J., and Wu, X., "Characteristics of Vortex Packets in Turbulent Boundary Layers," *Center for Turbulence Research*, 2010.

[37]Mathis, R., Hutchins, N., and Marusic, I., "Large-scale Amplitude Modulation of the Small-scale Structures in Turbulent Boundary Layers," *J. Fluid Mech.*, Vol. 628, 2009, pp. 311–337.

[38]Brown, G. L. and Thomas, A. S. W., "Large structure in a turbulent boundary layer," *Phys. Fluids*, Vol. 10, No. 2, 1977, pp. 243–251.

[39]Wang, X. and Silver, D., "Tracking and Visualizing Turbulent 3D Features," *IEEE Transactions on on Visualization and Computer Graphics*, Vol. 3, No. 2, 1997, pp. 129–141.

[40]Ozer, S., Silver, D., Bemis, K., Martin, M. P., and Takle, J., "Activity Detection for Scientific Visualization," *Large Data Analysis and Visualization (LDAV), 2011 IEEE Symposium*, 2011, pp. 117–118.

[41]Beekman, I., Priebe, S., Ringuette, M., and Martin, M. P., "Effect of Wall Temperature and Mach Number on the Turbulence Structure of Hypersonic Boundary Layers," *AIAA Paper No. 2009-1328*, Jan 2009.

[42]Liang, L., "User Manual for Object-Segmentation and Feature-Tracking (ostrk2.0) Using AVS/exp Package," Tech. rep., Rutgers, The State University of New Jersey, 2003.

[43]Thomas, A. S. W. and Bull, M. K., "On the role of wall-pressure fluctuations in deterministic motions in the turbulent boundary layer," *J. Fluid Mech.*, Vol. 128, 1983, pp. 283–322.

[44]Helm, C. and Martin, M. P., "Predictive Inner-Outer Model for Turbulent Boundary Layers Applied to Supersonic DNS," *AIAA Paper No. 2013-xxx*, Jan 2013.

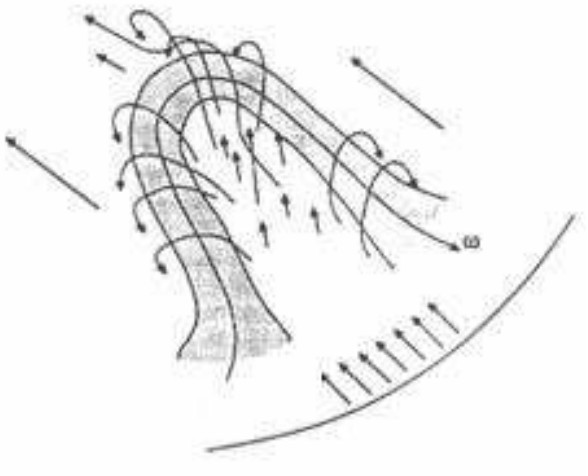

(a) Theodorsen's hairpin vortex.[1] The arrows on either side of the hairpin indicate the direction of the flow.

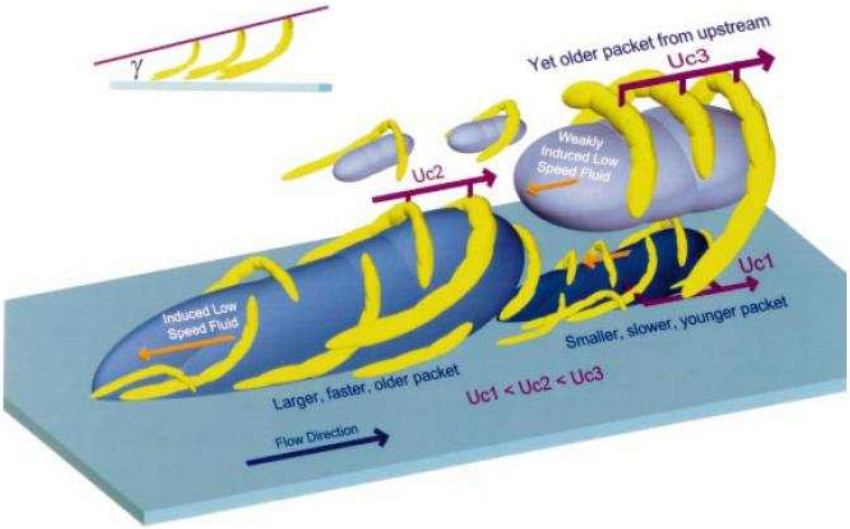

(b) Very large scale motion model of Adrian *et al.*[3] in which hairpin packets align to produce the long, low-momentum streaks in the logarithmic layer.

Figure 1. Coherent boundary layer structures. Figures from Theodorsen[1] and Adrian *et al.*[3]

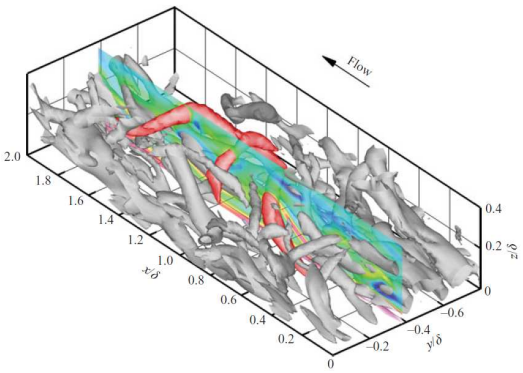

(a) Hairpin Packet conforming to the model of Adrian[3] found in a DNS data of Mach 3 turbulent boundary layer from Ringuette, Wu, and Martin.[25] See Figure 1(b).

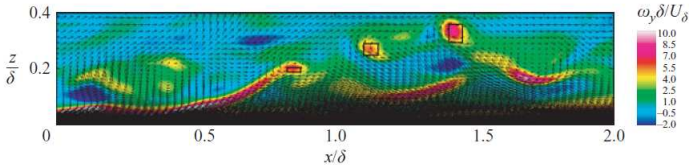

(b) A slice from (a) showing contours of spanwise vorticity, with boxes highlighting the hairpin vortex heads from Ringuette, Wu, and Martin.[25]

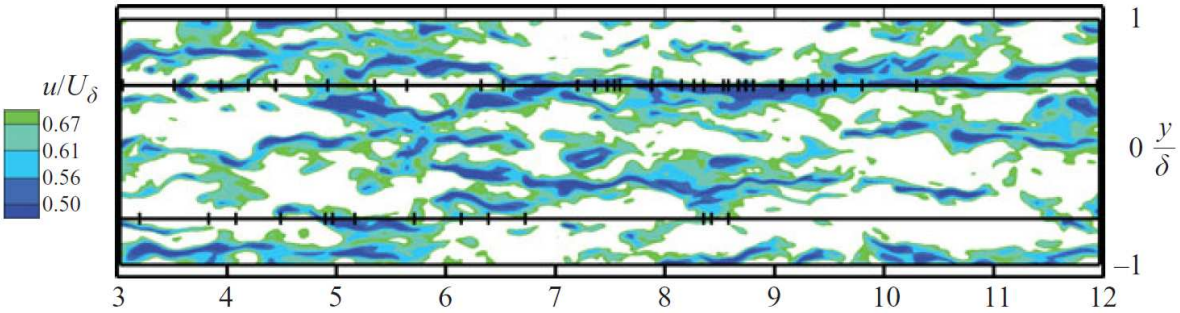

(c) Tickmarks indicating the presence of hairpin vortex packets found by searching two streamwise, wall-normal planes (indicated by the black lines) overlaying contours of streamwise velocity deficit in the logarithmic layer from Ringuette, Wu, and Martin.[25]

Figure 2. Figures reproduced from Ringuette, Wu, and Martin[25] conducted at the same Mach number, and slightly lower Reynolds number.

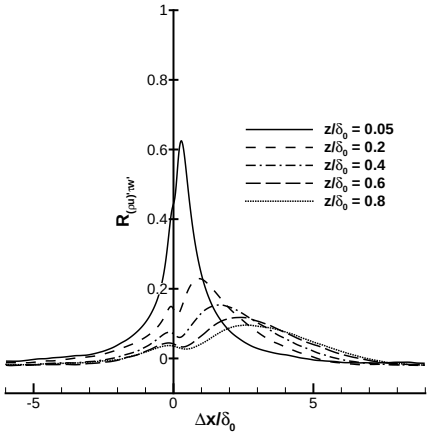

(a) Standard correlation profile for Mach 2.9 case.

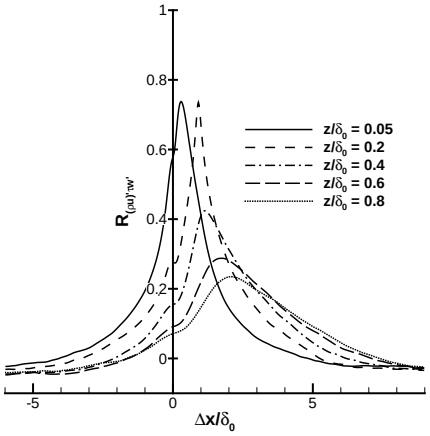

(b) Enhanced correlation profile for Mach 2.9 case.

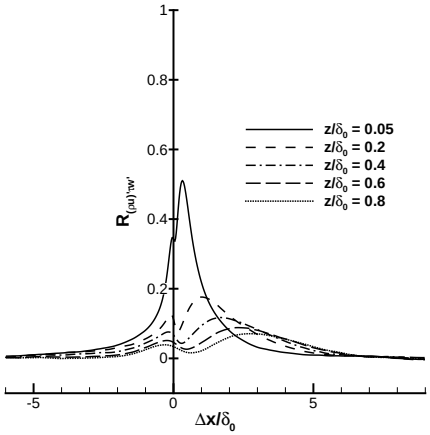

(c) Standard correlation profile for Mach 7.2 case.

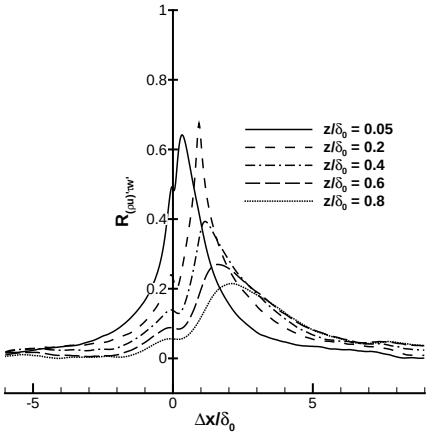

(d) Enhanced correlation profile for Mach 7.2 case.

Figure 3. Time-averaged spatial correlations between τ_w' and (ρu)' versus streamwise distance at different wall-normal distance for Mach 2.9 and Mach 7.2 cases.

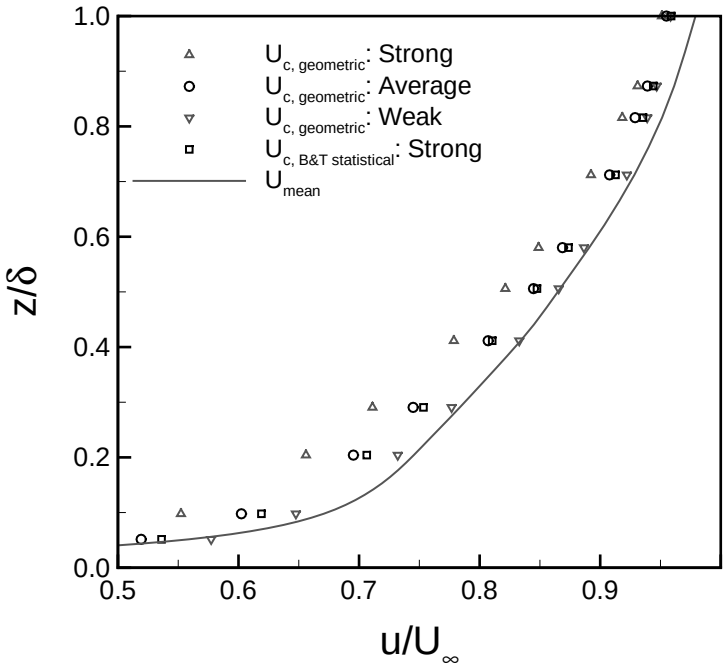

Figure 4. Vortex convection velocity profiles of Mach 3 DNS dataset by O'Farrell and Martin,[33] with the mean velocity profile as a solid line. The use of the 'geometric events' at the wall limit the correlation analysis to regions where ideal hairpin packets have been found, which correspond to the first three legend entries. The convection velocity determined from the 'strong' Brown and Thomas correlation[38] is plotted as a square symbol and is quite close in magnitude to the 'average' geometric convection velocity.

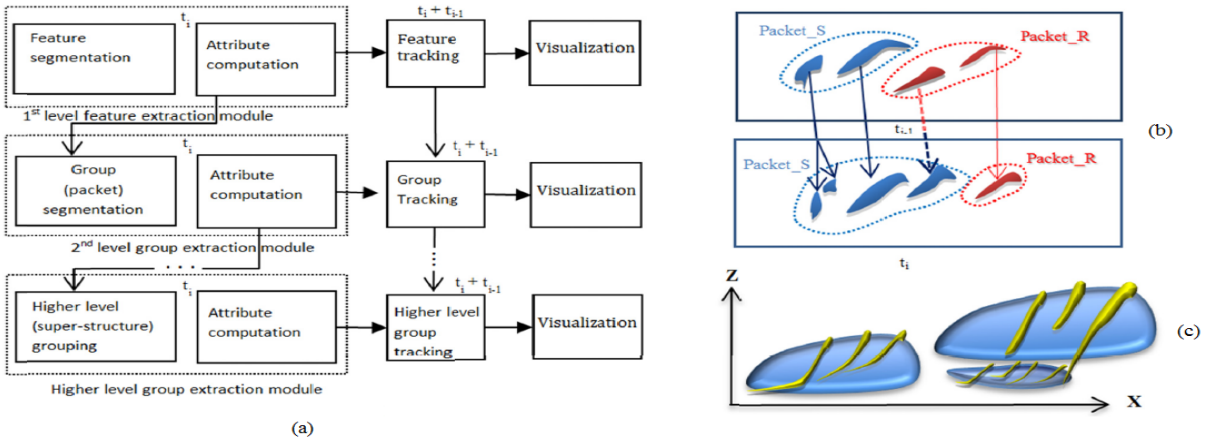

Figure 5. (a) Generalized tracking model that allows the tracking of packets and super-structures of packets of activity tracking algorithm;[40] (b) An illustration of activity tracking algorithm[40] where a feature moves from Packet_R to Packet_S. In Packet_S, within the iterative process, unphysical proliferation of packets is prevented; (c) An illustration of packets (formed of yellow hairpins) from activity tracking algorithm.[40] Three groups of packets are part of a larger packet.

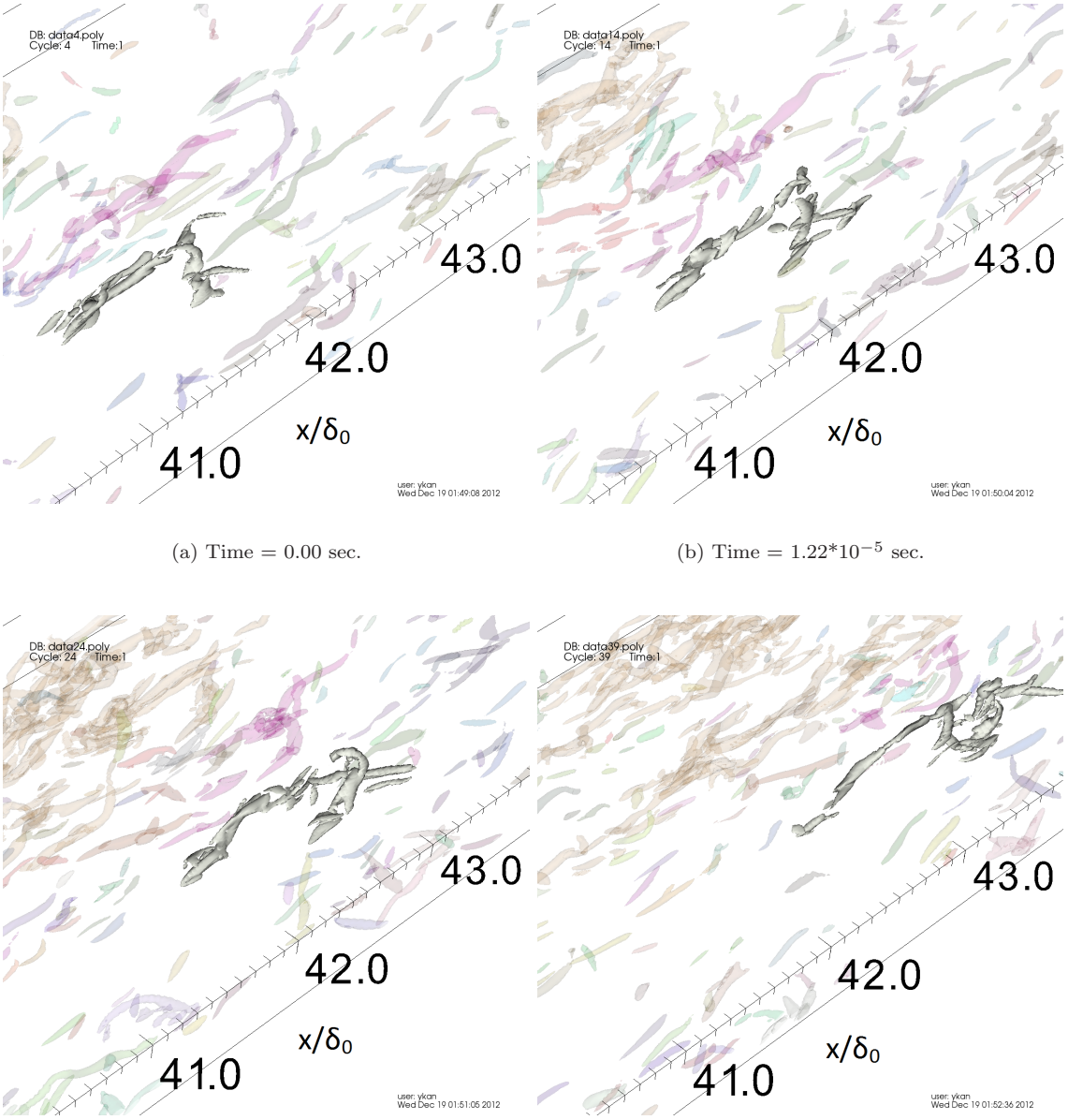

(a) Time = 0.00 sec.

(b) Time = $1.22*10^{-5}$ sec.

(c) Time = $2.24*10^{-5}$ sec.

(d) Time = $4.08*10^{-5}$ sec.

Figure 6. Temporally evolution of a geometrically 'strong' packet in the Mach 2.9 dataset in four different time realizations, where sampling rate is $1.20*10^{-6}$ sec. Other identified packets are shown at 90% translucency.

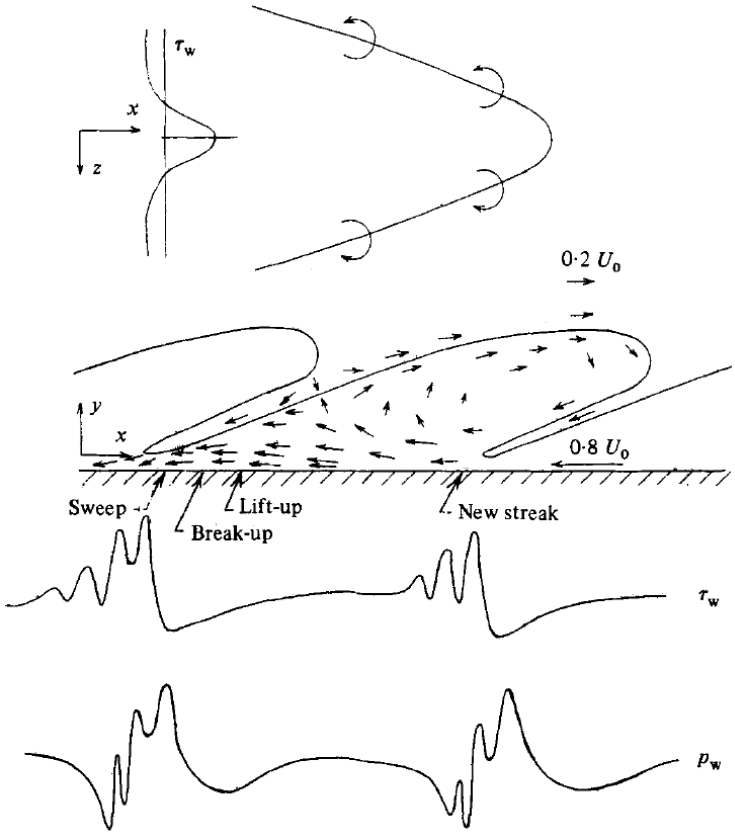

Figure 7. Model of organized structures in turbulent boundary layers from Thomas and Bull,[43] after Brown and Thomas,[38] as seen by an observer moving at $0.8U_0$.

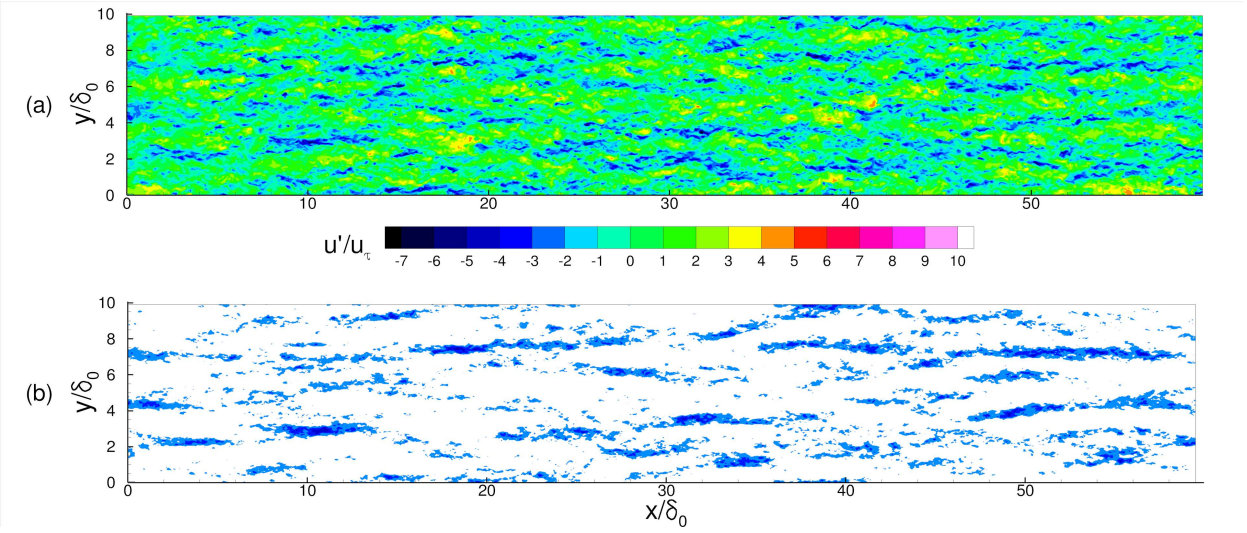

Figure 8. (a) Unfiltered snapshot of streamwise velocity fluctuation normalized by friction velocity in the logarithmic layer ($z/\delta_0 = 0.2$) for Mach 2.9 case. (b) Filtered snapshot of streamwise velocity fluctuation normalized by friction velocity after applying 3-dimensional POD in the logarithmic layer ($z/\delta_0 = 0.2$) for Mach 2.9 case.

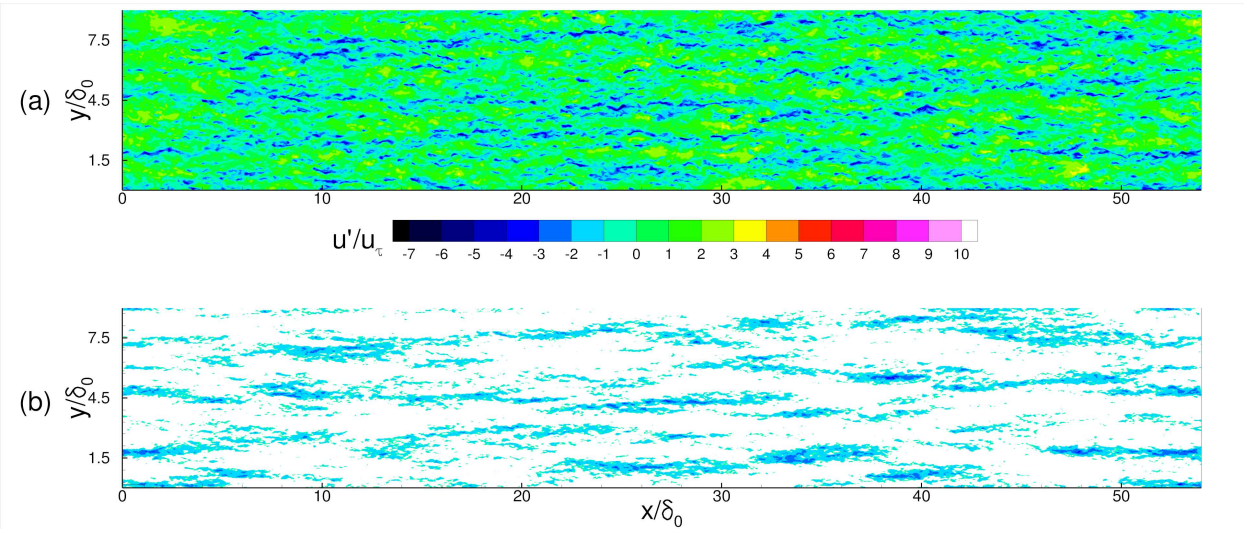

Figure 9. (a) Unfiltered snapshot of streamwise velocity fluctuation normalized by friction velocity in the logarithmic layer ($z/\delta_0 = 0.2$) for Mach 7.2 case. (b) Filtered snapshot of streamwise velocity fluctuation normalized by friction velocity after applying 3-dimensional POD in the logarithmic layer ($z/\delta_0 = 0.2$) for Mach 7.2 case.

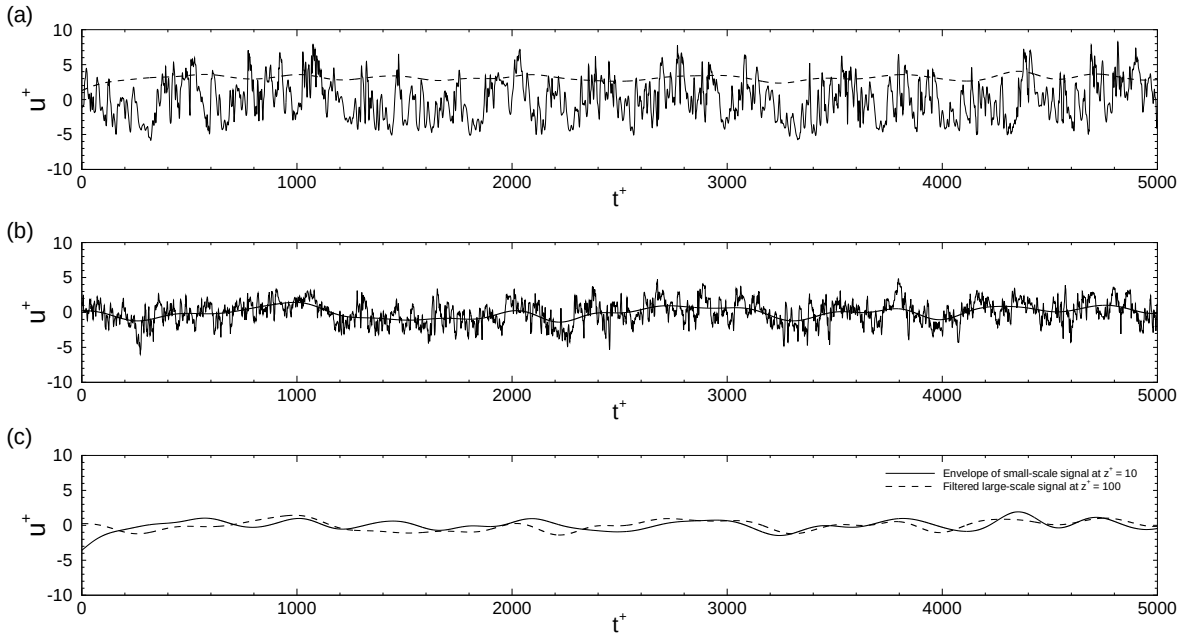

Figure 10. Example of modulation correlation between small-scales at $z^+ = 10$ and large-scales at $z^+ = 100$: (a) The small-scale signal at $z^+ = 10$ (solid line) and its envelope (dashed line); (b) The original and filtered large-scale signal at $z^+ = 100$; (c) The envelope of small-scale signal at $z^+ = 10$ (solid line) and the filtered large-scale signal at $z^+ = 100$ (dashed line).

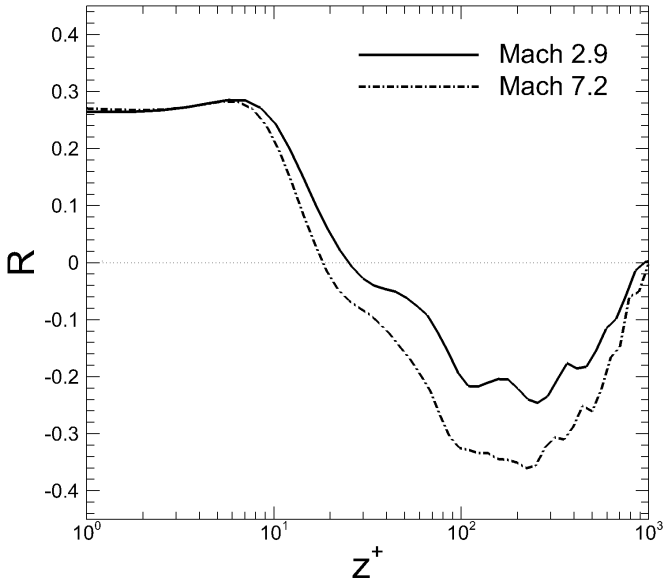

Figure 11. Modulation correlation coefficient profile large-scale outer signal and the small-scale envelope.

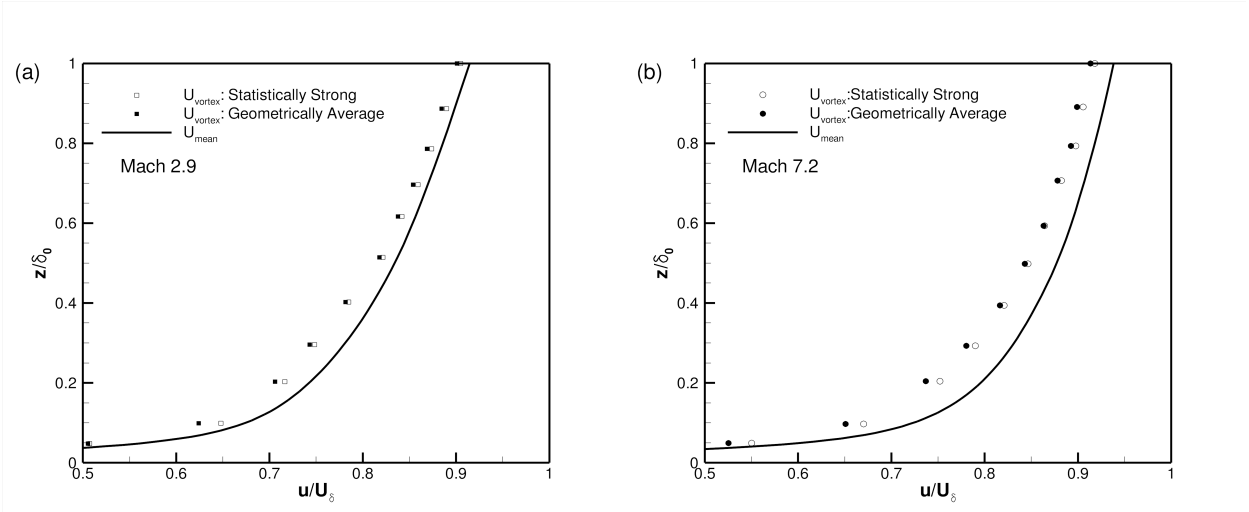

Figure 12. Average vortex convection velocity sample at streamwise station of $Re_\tau \approx 560$ versus distance from the wall computed using the 'strong,' and 'average' correlations of τ_w' and (ρu)'. (a) and (b) show the vortex convection velocity profiles of 'strong' statistical events and 'average' geometric events for the Mach 2.9 cases and the Mach 7.2 case, respectively.

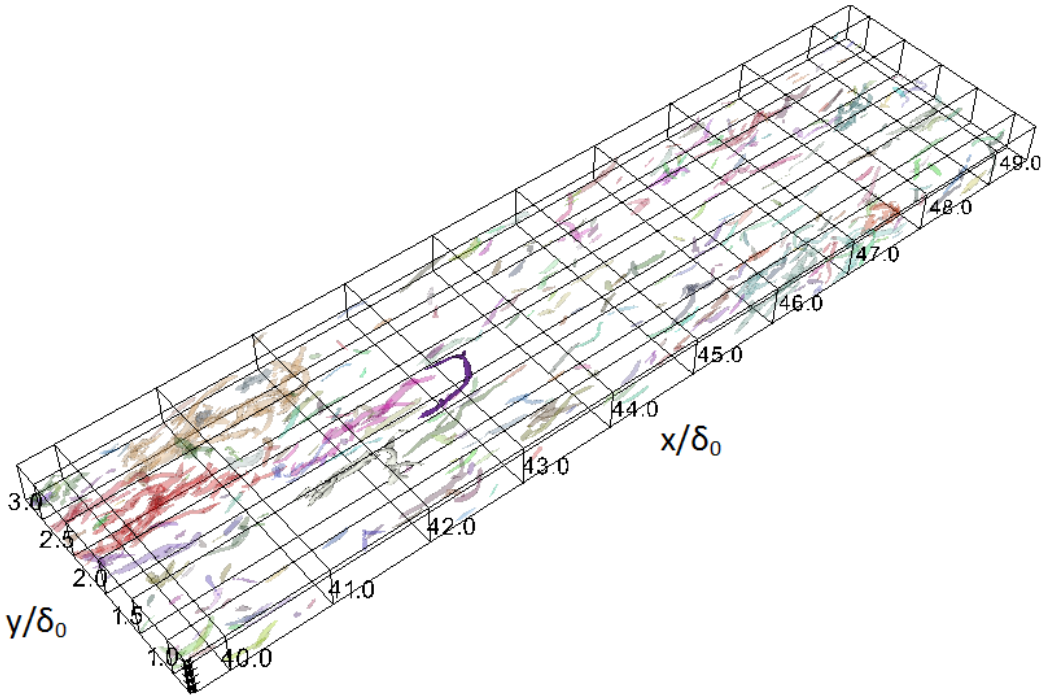

(a) Packets that are to be tracked are shown in solid color, where as other identified packets are shown at 90% translucency.

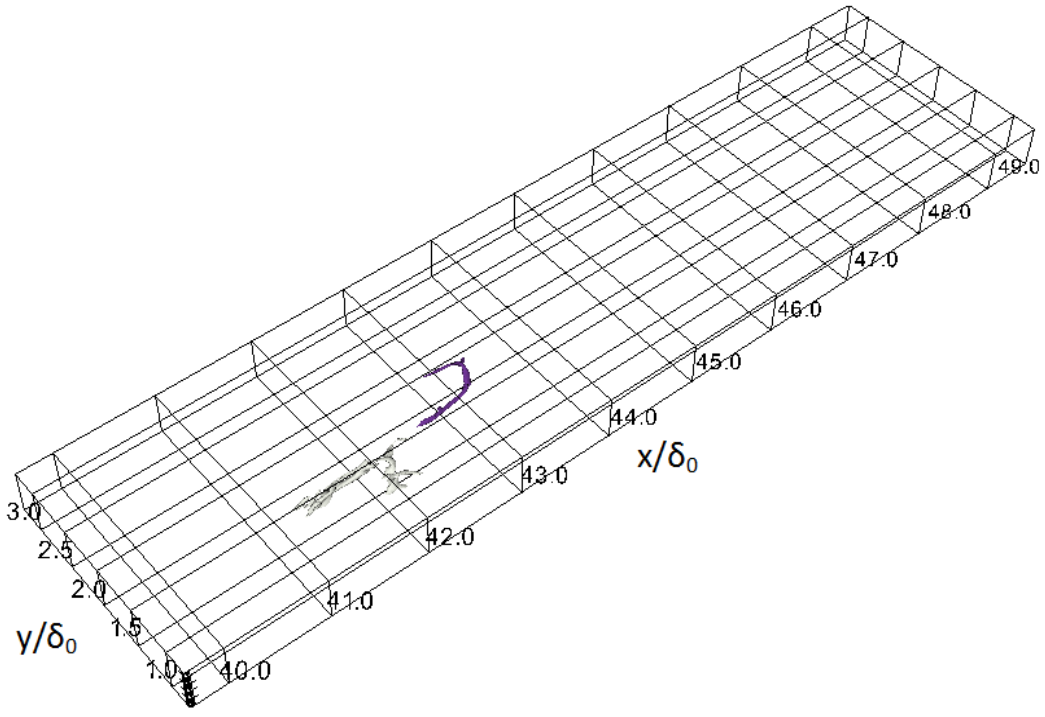

(b) Packets that are to be tracked are shown only.

Figure 13. Two hairpin packets tracked in the DNS data of Mach 2.9 turbulent boundary layer. Structures are visualized by an iso-surface of swirling strength at $4.5\overline{\lambda_{ci}^2}$. Both packets and their wall signatures are subsequently tracked are identified in Figure 14 and Figure 15.

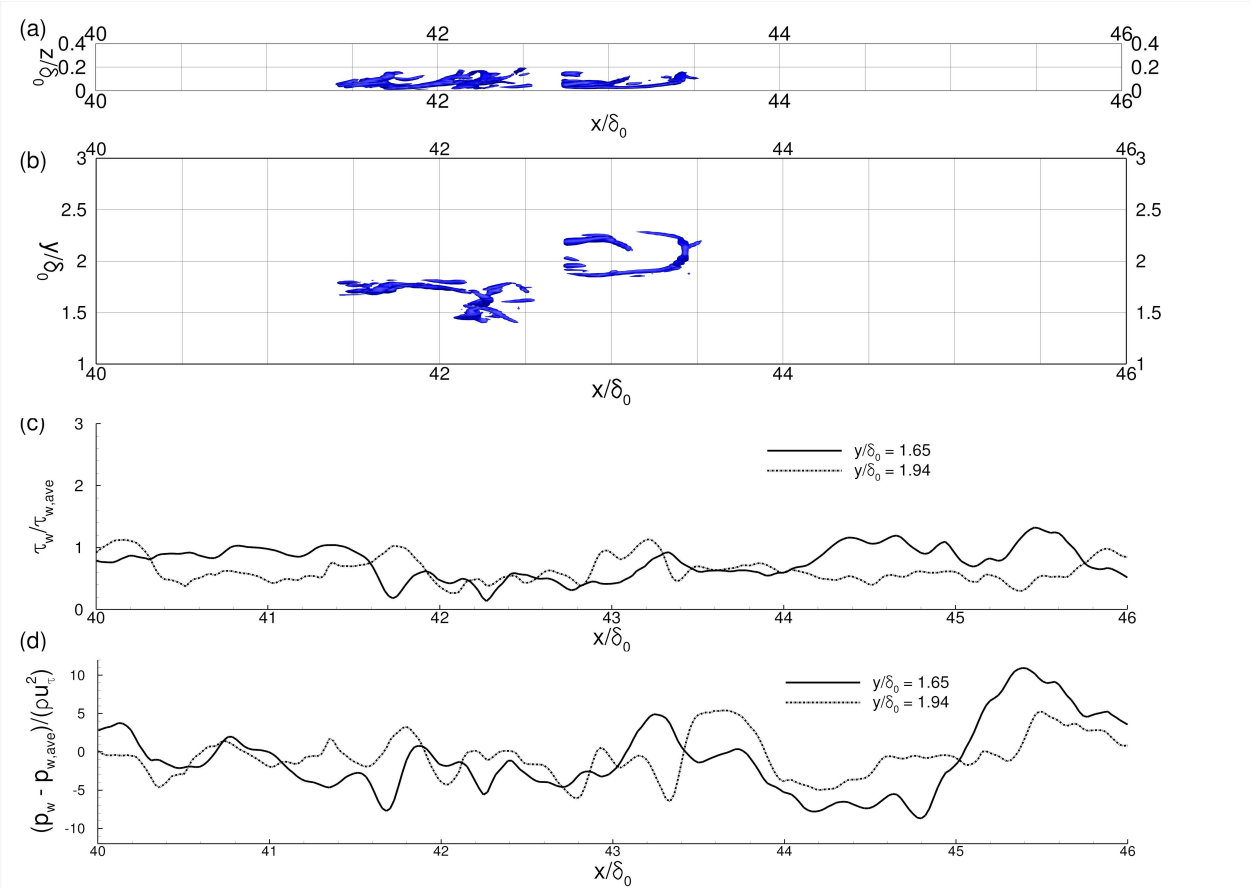

Figure 14. Wall-shear stress and wall-pressure signatures of two geometrically 'strong' hairpin packets in the DNS data of Mach 2.9 turbulent boundary layer. (a) and (b) show the streamwise-wall normal plane and streamwise-spanwise plane, respectively, over two packets, visualized by the iso-surface of swirling strength at $\lambda_{ci}^2 = 4.5\overline{\lambda_{ci}^2}$. (c) and (d) plot the wall-shear stress and wall-pressures signals along the mid-span of the hairpin packets.

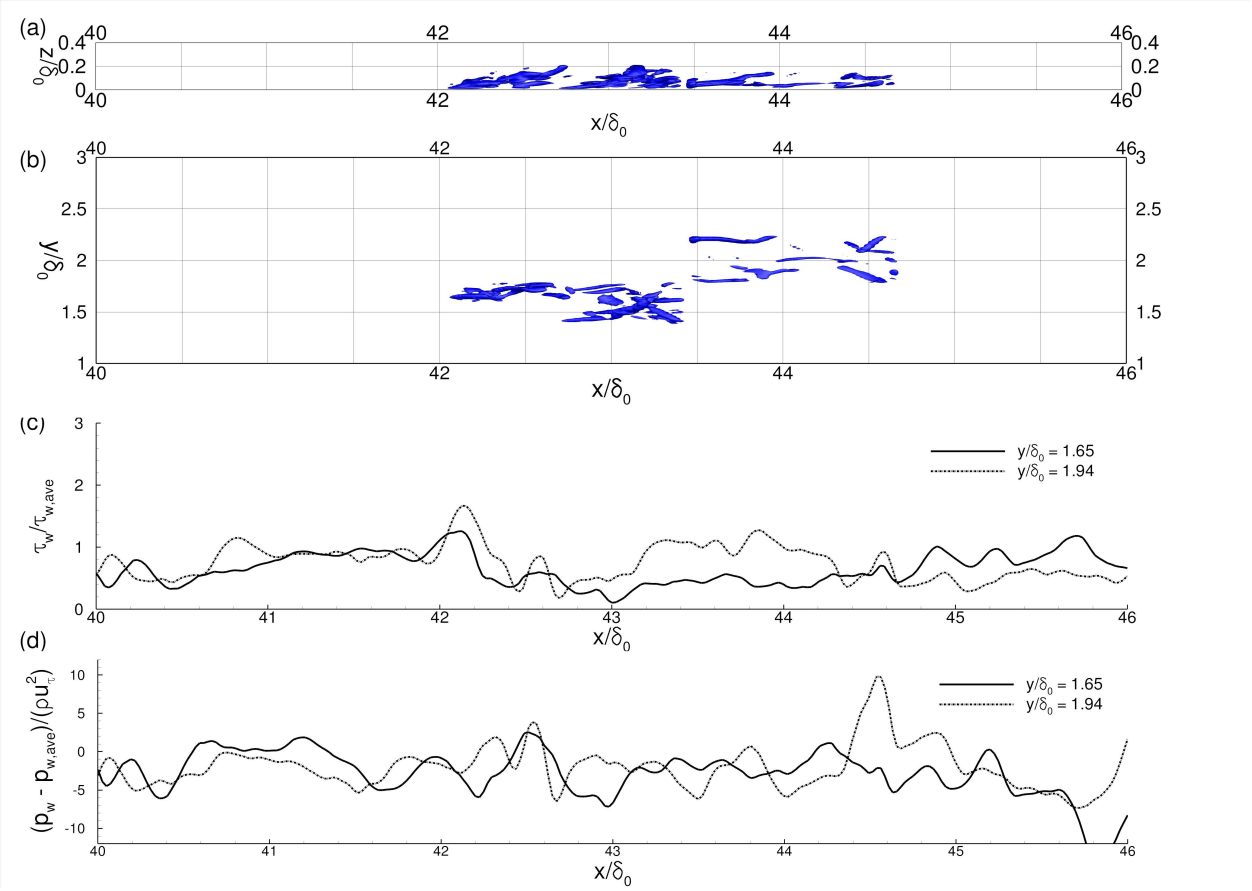

Figure 15. Same plot as Figure 14 but at later timestep where both packets travel a distance of approximately δ_0.

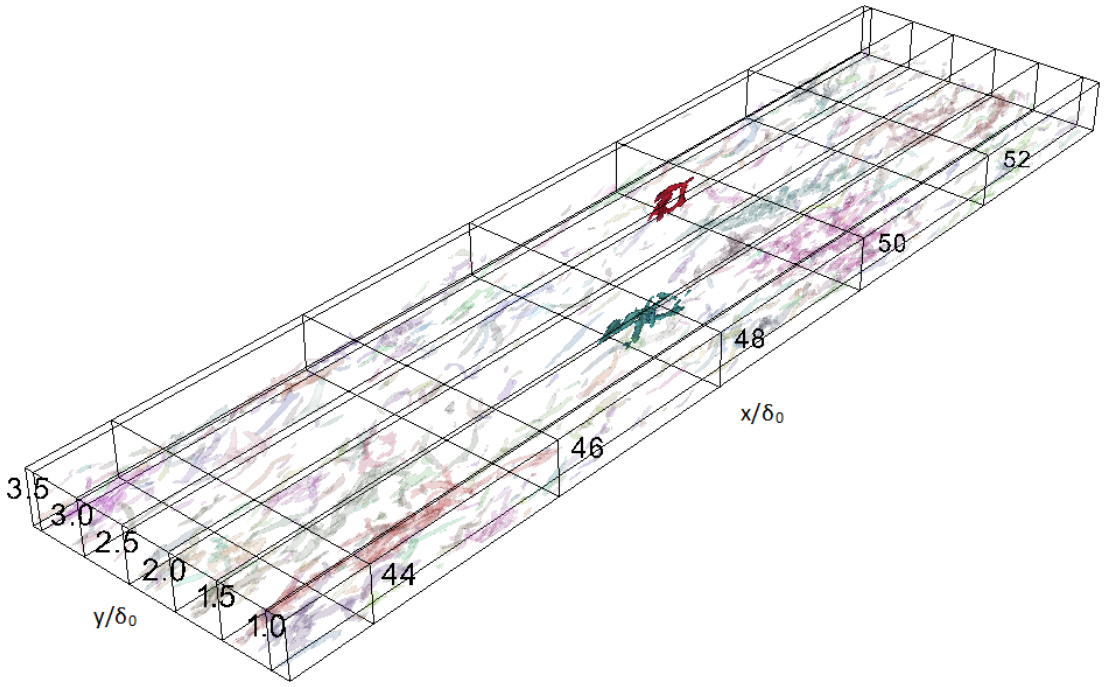

(a) Packets that are to be tracked are shown in solid color, where as other identified packets are shown at 90% translucency.

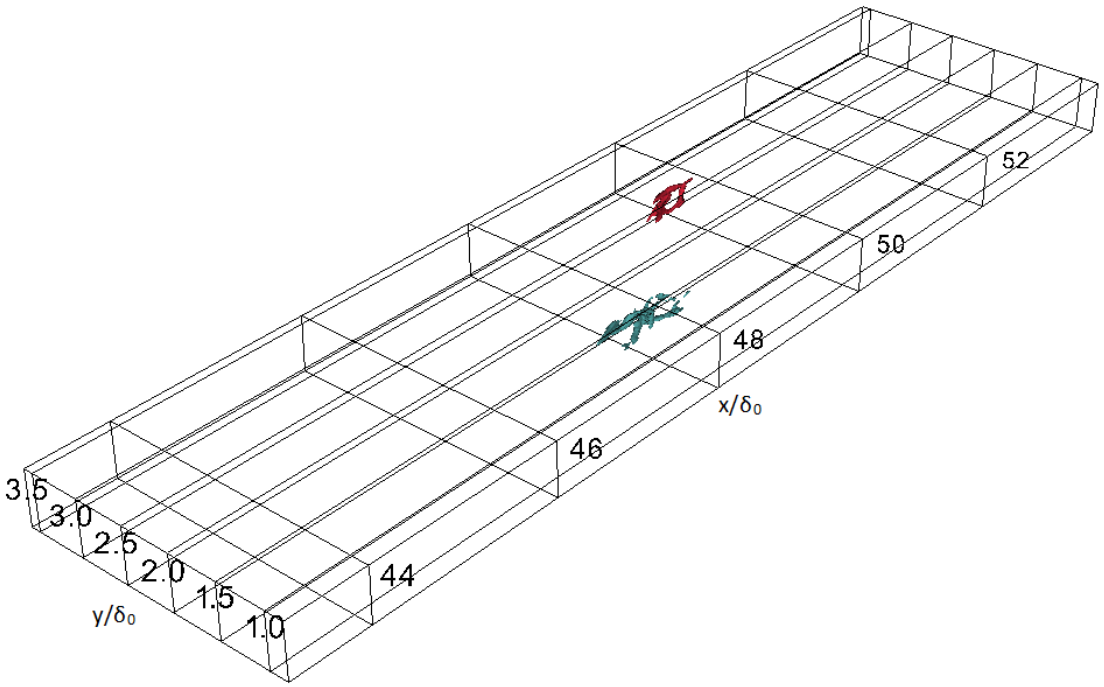

(b) Packets that are to be tracked are shown only

Figure 16. Two hairpin packets tracked in the DNS data of Mach 7.2 turbulent boundary layer. Structures are visualized by an iso-surface of swirling strength at $4.5\overline{\lambda_{ci}^2}$. Both packets and their wall signatures are subsequently tracked are identified in Figure 17 and Figure 18.

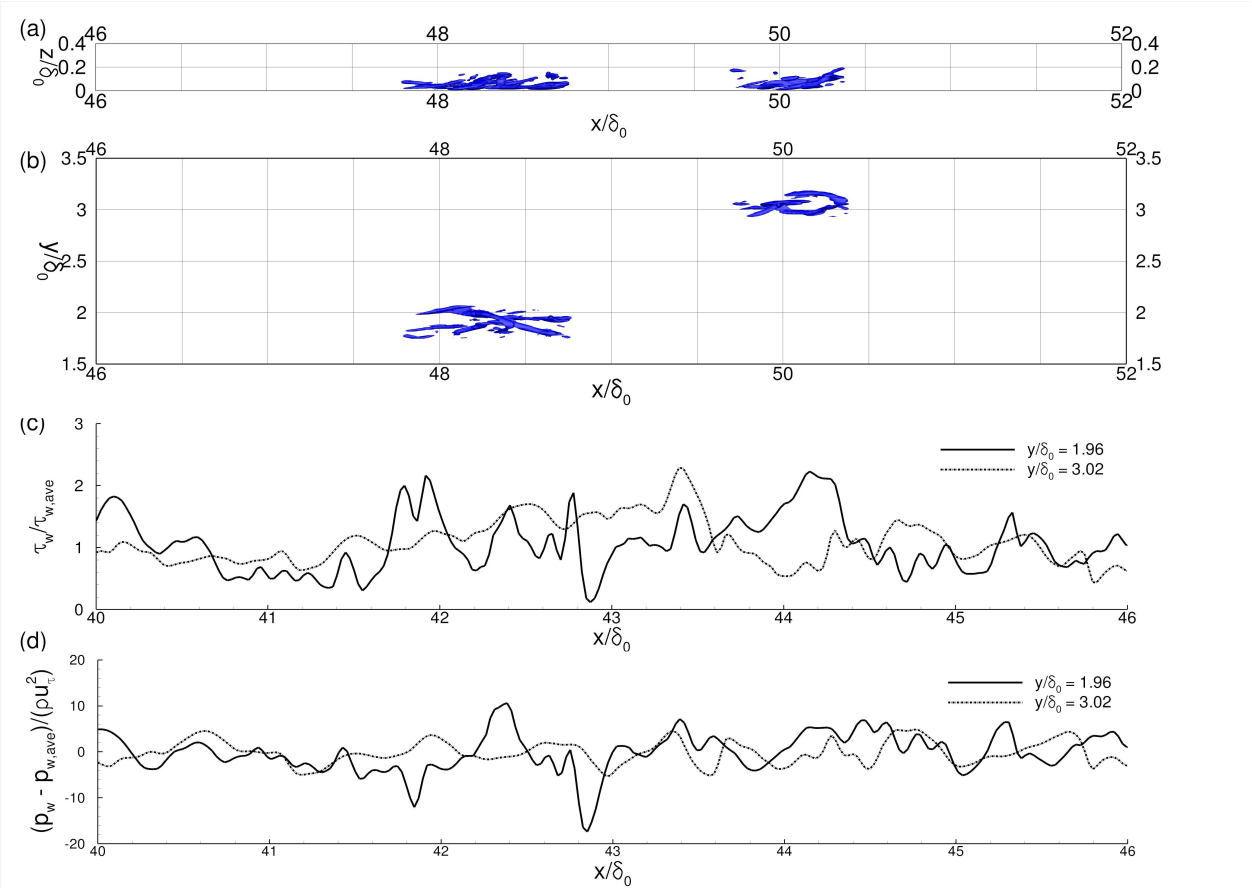

Figure 17. Wall shear stress and wall-pressure signatures of two geometrically 'strong' hairpin packets in the DNS data of Mach 7.2 turbulent boundary layer. (a) and (b) show the streamwise-wall normal plane and streamwise-spanwise plane, respectively, over two packets, visualized by the iso-surface of swirling strength at $\lambda_{ci}^2 = 4.5\overline{\lambda_{ci}^2}$. (c) and (d) plot the wall-shear stress and wall-pressures signals along the mid-span of the hairpin packets.

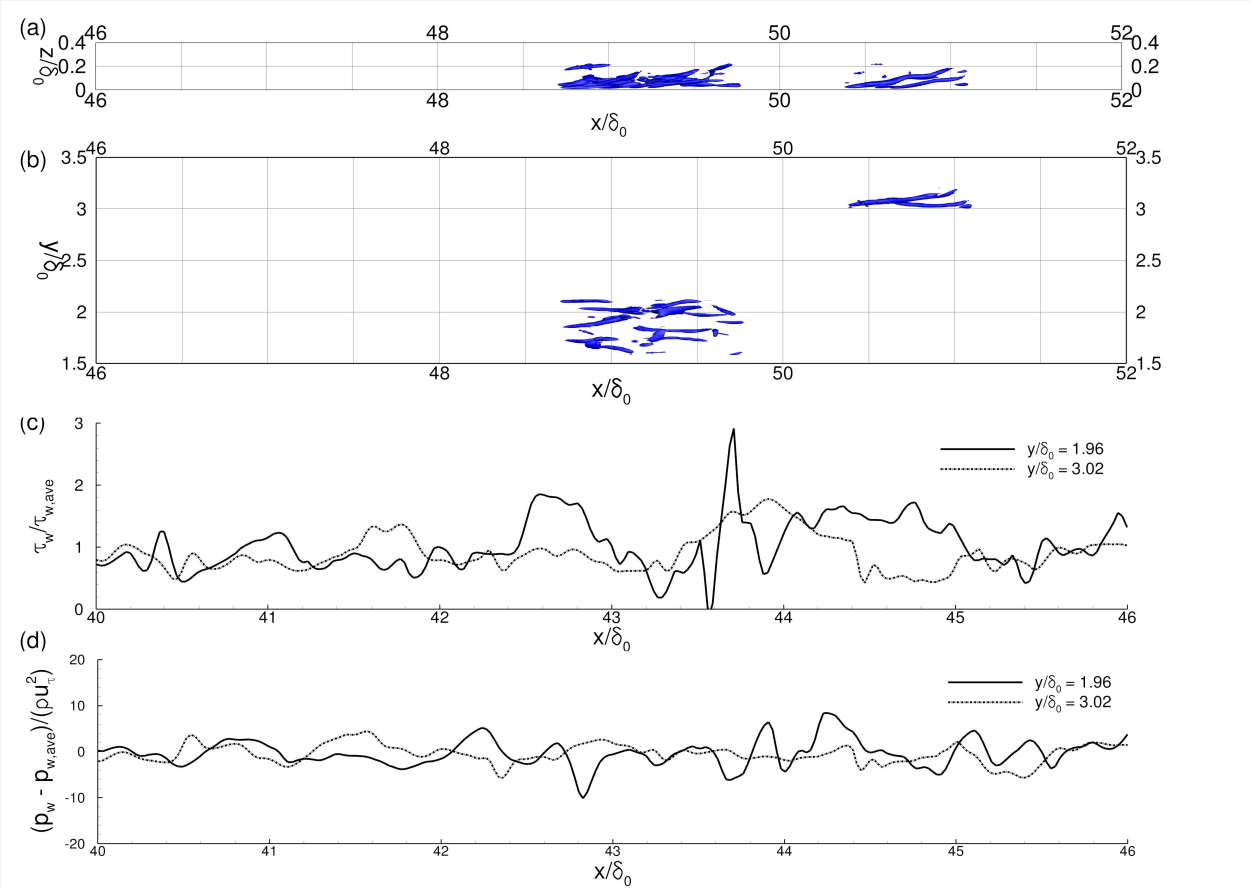

Figure 18. Same plot as Figure 17 but at later timestep where both packets travel a distance of approximately δ_0.